PROCEEDINGS, Thirty-Eighth Workshop on Geothermal Reservoir Engineering
Stanford University, Stanford, California, February 11-13, 2013
SGP-TR-198

APPLICATIONS OF RADAR INTERFEROMETRY TO DETECT SURFACE DEFORMATION IN GEOTHERMAL AREAS OF IMPERIAL VALLEY IN SOUTHERN CALIFORNIA

Mariana Eneva[1], David Adams[1], Giacomo Falorni[2], and Jessica Morgan[2]

[1]Imageair Inc., 600 Greensburg Circle, Reno, Nevada 89509, U.S.A., e-mail: meneva@imageair-inc.com
[2]TRE Canada Inc., 475 W. Georgia Street, Suite #410, Vancouver, BC V6B 4M9, Canada

ABSTRACT

InSAR (interferometric synthetic aperture radar) is applied in Imperial Valley of southern California to detect and characterize surface deformation in existing geothermal fields, possible future geothermal developments, and around faults. The data used are from the Envisat satellite, collected over the period 2003-2010. The specific InSAR technique applied, SqueeSAR^{TM}, identifies permanent and distributed scatterers (PS and DS), which play the role of numerous benchmarks throughout the study area. Deformation time series are obtained at thousands of individual scatterer locations. Their slopes represent the annual deformation rates. The technique is particularly suitable for vegetated and rural areas, thus providing results from the agricultural lands of Imperial Valley, where conventional InSAR methods have not worked before. The SqueeSAR results are first obtained in the line-of-sight (LOS) to the satellite. Using measurements from two geometries, ascending and descending, makes it possible to decompose the two LOS movements into vertical and horizontal displacements.

Significant subsidence is observed at all geothermal fields operating during the period of satellite data (2003-2010). These include the CalEnergy units of the Salton Sea geothermal field, and Ormat's Heber and East Mesa geothermal fields. At Heber, uplift is also detected in an area adjacent to the subsidence. The results from SqueeSAR are in agreement with the ground-based measurements from the annual leveling surveys carried out at both Salton Sea and Heber. Regional GPS data and relocated earthquakes are also used to inform our analysis results. Furthermore, baseline surface deformation is detected at sites, where production either started after, or at the end of the period covered by satellite data. These are Hudson Ranch – I at the Salton Sea geothermal field (operated by Energy Source since early 2012) and North Brawley (operated by Ormat since 2010). The baseline at sites of geothermal potential is also determined, such as areas of interest to the U.S. Navy Geothermal Program Office and Orita (formerly East Brawley). In addition, the SqueeSAR measurements reveal differential movements on both sides of faults, clearly marking the Superstition Hills and Imperial faults, as well as parts of the San Andreas fault. The surface displacements are attributed to the ongoing regional extension due to the relative movements of the North American and Pacific plates, as well as to localized tectonic deformation associated with fault networks, pull-apart basins, and rotational blocks. Finally, we observe effects caused by an October 2006 aseismic event on the Superstition Hills fault, and by a M7.2 earthquake that occurred south of the U.S. – Mexico border in April 2010.

We conclude that InSAR provides unprecedented information on surface deformation in Imperial Valley, as long as suitable techniques, such as SqueeSAR^{TM}, are used to tease out signals amidst the extensive agriculture. Such observations can be effectively used for pre-production reservoir assessment, feedback to mitigate any environmental impact that might occur at operating fields, and exploration efforts to identify suitable drilling targets.

BACKGROUND

Regional Setting

The Imperial Valley extends for about 80 km in southern California, from the southern shore of the Salton Sea toward the U.S. – Mexico border (Figure 1). Together with the Coachella Valley to the north, it is part of the Salton Trough, which is a spreading center associated with the relative movement of the Pacific and North American Plates. Thus it is characterized by active tectonics, with both subsidence and substantial horizontal movements taking place on a regional scale. This is confirmed by current observations at the GPS stations in the region (Fig. 1). Local sources of deformation are represented by blocks formed by networks of strike-slip and normal faults, many of which do not have surface expression, especially in the agricultural areas. The contribution of local tectonics is likely significant, especially in light of recent studies using seismic

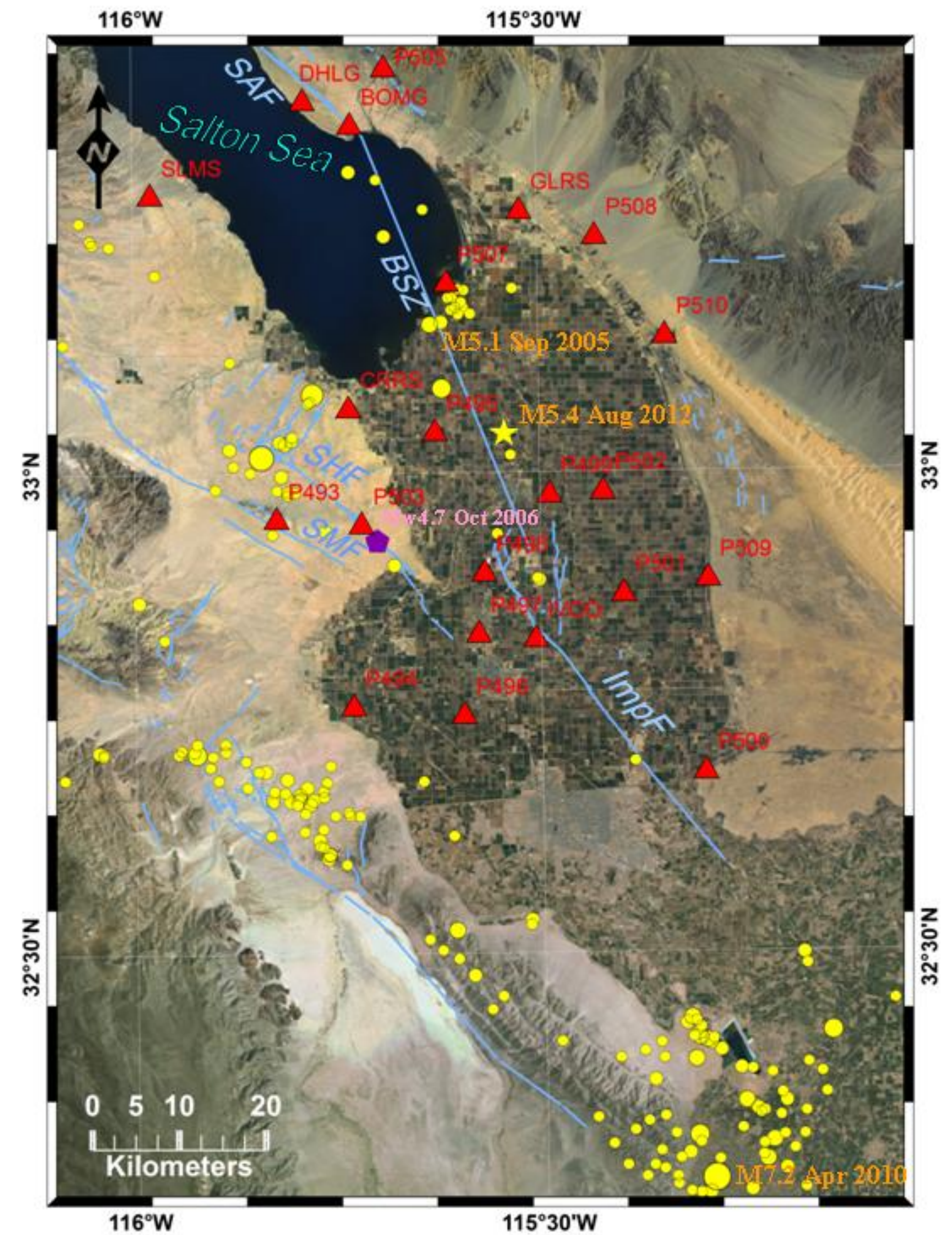

Figure 1. Map of the study area, superimposed on a satellite image. Red triangles mark GPS stations. Yellow circles denote epicenters of M $\geq$ 4.0 earthquakes occurring between 1981 and mid-2011 (relocated by Hauksson et al. 2012); circle size increases with magnitude. Earthquakes of importance for the study period (2003-2010) are labeled with orange letters and numbers. The epicenter of a M5.4 swarm in August 2012 is marked with a yellow star, to indicate that it occurred outside the period of the relocated catalog. An October 2006 aseismic event, labeled with pink letters and numbers, was detected by a creep meter (purple pentagon next to GPS station P503). Blue traces denote faults (source U. S. Geological Survey): SAF (San Andreas fault); ImpF (Imperial fault); SHF (Superstition Hills fault); SMF (Superstition Mountain fault); and BSZ (Brawley Seismic Zone – marked with straight line through its center).

reflection data collected from the Salton Sea, as reported by Brothers et al. (2009). These authors note that oblique extension across strike-slip faults causes subsidence, leading to the formation of pull-apart basins, such as the Salton Sea and surrounding areas. They project maximum subsidence near the southern shoreline of the lake, approximately coincident with the locations of Quaternary volcanism and a northeast-trending band of very high heat flow.

In addition to the gradual deformation due to regional and local tectonics, the Salton Trough experiences abrupt surface ruptures due to large earthquakes and associated aseismic slip. The Brawley Seismic Zone (BSZ) represents the transitional zone between the southern tip of the San Andreas fault to the northeast, and the Imperial fault to the south (Fig. 1). It likely includes a number of faults, but they do not have obvious surface expression. Some of these may be related to linear features, as suggested by map displays of relocated earthquakes (Hauksson et al., 2012) and depth cross-sections (see examples below and in Eneva et al., 2009; Eneva and Adams, 2010, and Eneva et al., 2012). Brothers et al. (2009) attribute the larger earthquakes ($M \geq 6$) to the accommodation of the regional extension and subsidence, and the smaller events ($M < 5$) and microseismicity to fracturing and block rotation within narrow (< 5-km-wide), dextral shear zones. Seismic swarms, such as those in 1981, 1989, 2005, 2009, and 2012 have been related to the high heat flow in the region (Ben-Zion and Lyakhovsky, 2006). During the study period (2003-2010), a M5.1 swarm occurred on the territory of the Salton Sea geothermal field, which was studied in great detail by Lohman and McGuire (2007). A M5.4 swarm occurred in August 2012 in the area of Brawley, following the study period. Both epicenters are marked in Fig. 1, as well as relocated $M \geq 4$ events for the period January 1981 – June 2011 (Hauksson et al., 2012). Many of these events were aftershocks of an April 2010 M7.2 event south of the border, also marked in Fig. 1.

Aseismic creep has been detected on many occasions in Imperial Valley, usually triggered by larger earthquakes in the region and the wider vicinity (e.g., Rymer et al., 2002). The most notable example during the study period (2003-2010) is the wide-spread triggered slip on faults in the Imperial Valley by the April 2010 M 7.2 event (Wei et al., 2011). In addition, an October 2006 aseismic event of equivalent moment magnitude Mw4.7 was detected by a creep meter on the Superstition Hills fault, and was confirmed by satellite interferometry (InSAR) and field measurements (Wei et al., 2009). This event occurred without triggering by a larger earthquake.

Study Areas

The surface deformation on the territory of several areas of total size larger than 2,300 km^2 is studied in Imperial Valley (Figure 2). The high heat flow in the Salton Trough is associated with a number of geothermal resources. The study region includes several currently operating geothermal fields. The largest one is Salton Sea (SSGF), marked with #1 in Fig. 2. It has been operated by CalEnergy Generation for more than 30 years. In early 2012 Energy Source LLC started a new development (Hudson Ranch - I, also known as Featherstone plant), with more plants to come on line. The other operating fields are Heber (HGF), North Brawley (NBGF), and East Mesa (EMGF), operated by Ormat Technologies Inc. These areas are marked with #2, #3 and #4 in Fig. 2. Other sites are of potential geothermal interest to the U. S. Navy Geothermal Program Office (GPO) - these are the areas of Superstition Hills and Superstition Mountain faults to the west (#5 in Fig. 2) and the Hot Springs fault and Chocolate Mountains to the northeast (#6 in Fig. 2). Orita (also known as East Brawley), to the east of NBGF, has been formerly of interest to Ram Power - it is marked by #7 in Fig. 2. In addition to these known geothermal resources, areas along faults are also studied, such as the San Andreas fault (#8 in Fig. 2) and Imperial fault (#9 in Fig. 2). The overall purpose of our work is to analyze and interpret the surface deformation in all of these areas, both in terms of ongoing tectonic activity and possible effects of the operation of the fields.

Method and Techniques

The method used for mapping surface deformation in Imperial Valley is satellite radar interferometry, also known as interferometric synthetic aperture radar (InSAR). The traditional InSAR technique used for detecting deformation from earthquakes, water pumping, mining, and some geothermal areas, has been differential InSAR (DInSAR) (e.g., see Eneva, 2010 for an overview). In particular, there have been DInSAR observations at some geothermal fields, such as East Mesa in southern California (Massonnet et al., 1997), fields in Nevada (e.g., Oppliger et al., 2008), Coso in eastern California (Wicks et al., 2001; Fialko and Simmons, 2000), and Cerro Prieto in Mexico (Carnec and Fabriol, 1999) south of the study area. However, DInSAR does not work in agricultural areas like Imperial Valley. For such areas, a recent innovation, PSInSAR™ (Ferretti et al., 2000, 2007) is needed. It makes use of so-called "permanent scatterers" (PS) to produce detailed deformation time series and deformation rates derived from those time series. PS are objects, such as buildings, fences, lampposts, transmission towers, rock outcrops, points aligned along roads and canals,

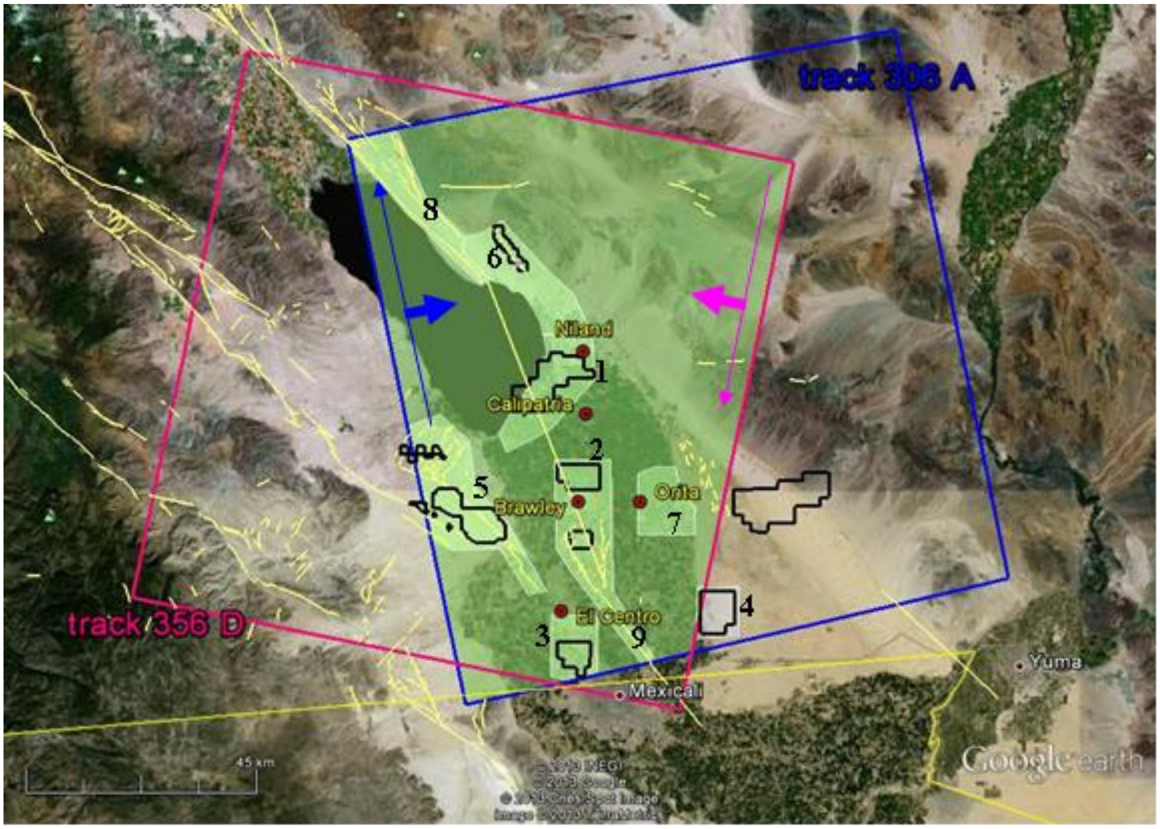

Figure 2. Google Earth map showing footprints of satellite scenes and studied areas. Footprints of Envisat scenes are outlined with pink (descending track 356) and blue (ascending track 306). Thin arrows show satellite movement from north to south (descending) and from south to north (ascending). Thick arrows show viewing direction (right-looking, perpendicular to satellite movement). Green area shows overlap between the two geometries. Current and some prospective geothermal areas are shown with black polygons. Areas of interest are shown with transparent white polygons, including the following: current geothermal fields (1-Salton Sea, 2-North Brawley, 3-Heber, and 4-East Mesa); some of the prospective geothermal areas (5-Superstition Hills, 6-Hot Springs Fault/Chocolate Mountains, 7-Orita); and fault areas of interest (8-southern portion of San Andreas fault, and 9-Imperial fault).

etc., which serve as reflectors of the radar waves. Many of the PS in the agricultural areas of Imperial Valley are aligned along roads and canals. We have previously applied the PSInSAR™ technique in the Salton Sea geothermal field, using two-year data from a Canadian satellite, Radarsat (Eneva et al., 2009; Eneva and Adams, 2010; Falorni et al., 2011).

The latest improvement of PSInSAR™, called SqueeSAR™ (Ferretti et al., 2011), ads to the PS so-called "distributed scatterers" (DS). These are homogeneous areas emitting signals with smaller signal-to-noise ratios than the PS, but still significantly above the background. These include rangelands, pastures, and bare earth characteristic of relatively arid environments. This technique is particularly well suited to study rural areas. We have successfully applied SqueeSAR™ for the San Emidio geothermal field in northwestern Nevada (Eneva et al., 2011) and again to the Salton Sea geothermal field (Eneva et al., 2012) using data from the European Envisat satellite collected over an 8-year period.

Displacement measurements with SqueeSAR are done relative to a reference point, considered to be stable. This is similar to choosing one of a set of leveling benchmarks as a reference (datum) point when performing leveling surveys. Thus only relatively local movements are measured with SqueeSAR, rather than regional ones. This has to be kept in mind when viewing the SqueeSAR results, because depending on the reference point, the displacements may be of different amounts, although overall relative patterns of deformation would remain the same. It is hard to find "motionless" reference points in tectonically active regions like the Salton Trough. Therefore it is useful to know the absolute movements of the reference points. This can be achieved by striving to use, where possible, locations of GPS stations as a reference.

Table 1. Information on some of the GPS stations: period of operation, three-component rates in mm/year, times of offsets associated with earthquakes, and amounts of offsets.

GPS Stat	Time period	Rate N	Rate E	Rate U	Time Offset	Offset N	Offset E	Offset U
DHLG	1999.7904 - 2005.6699	-0.1	-22.4	-1.0	2005.6699	0.7	-0.8	0.5
	2005.6699 - 2012.7063	-1.4	-22.7	0.7	2010.2589	-19.3	2.5	4.7
GLRS	2000.8292 - 2005.6699	-6.8	-16.1	-1.1	2005.6699	-1.0	-1.8	0.0
	2005.6699 - 2012.7063	-9.1	-17.0	0.9	2010.2589	-26.6	3.2	6.5
P493	2007.7411 - 2012.7063	8.1	-32.5	0.9	2010.2589	-50.5	5.1	9.7
P496	2005.8589 - 2012.7063	23.6	-39.3	4.9	2010.2589	-196.1	30.5	11.3
P497	2006.0288 - 2012.6844	10.4	-26.1	1.9	2010.2589	-112.9	15.5	20.9
P498	2005.2507 - 2012.6516	8.7	-23.9	-2.9	2010.2589	-83.8	10.5	19.7
P500	2005.3027 - 2012.7063	-2.8	-14.2	0.4	2010.2589	-71.1	68.6	10.1
P503	2007.3932 - 2012.7008	8.6	-28.6	0.3	2010.2589	-76.7	16.3	12.9
P507	2005.7192 - 2012.7063	-12.4	-20.8	-14.6	2010.2589	-36.4	5.1	8.6

The deformation is first measured in the line-of-sight (LOS) to the satellite. The LOS movements are negative when their direction is away from the satellite and positive toward the satellite. When the look angle is steep, the LOS movements are rather representative of the vertical displacements. Thus a LOS movement away from the satellite is often indicative of relative subsidence and toward the satellite – of uplift. The availability of scenes, where the satellite moves north to south (descending) and south to north (ascending), makes it possible to decompose the two sets of LOS movements into vertical and horizontal components.

Satellite Data

Two sets of radar scenes from the European Envisat satellite are used in this analysis. The data were obtained from the European Space Agency (ESA). One data set consists of 45 descending images from track 356, covering the period February 7, 2003 – September 3, 2010. The other one consists of 33 ascending images from track 306, covering the period December 16, 2003 – August 21, 2010 (39 scenes are available, but 6 turned out to be unsuitable for the analysis). The footprints of the two sets are marked on Fig. 2. The look angles toward the ground, (i.e., measured from the vertical to the ground), are 21^0 to 22^0 for the descending images, and 20^0 to 21^0 for the ascending images. The viewing directions (right-looking from the satellite) are west-northwest (WNW) for the descending scenes and east-northeast (ENE) for the ascending scenes, as marked with thick arrows in Fig. 2. The sensitivity of the movements detected in the line-of sight (LOS) is measured with values between 0 and 1, with larger values indicating greater sensitivity. Because of the steep look angles, the LOS movements are representative of the vertical surface deformation, with sensitivity ~0.93 for both the descending and ascending images. The sensitivity to the west-east horizontal component of surface deformation is ~0.34-0.37, while the sensitivity to the south-north component is negligible (~0.07-0.08).

Other Data

The surface deformation measured by SqueeSAR is compared, or superimposed with, other data where possible. These include leveling data (i.e., vertical measurements) for the Salton Sea geothermal field (provided by CalEnergy) and the Heber geothermal field (provided by the Imperial County Department of Public Works – ICDPW). The SSGF leveling data set consists of leveling time series from approximately annual surveys in the period 1998-2012, at 79 benchmarks (not all have been used during each annual survey). The reference point for the surveys is a benchmark on the Salton Sea shore, Obsidian Butte (S-1246).

The list provided by ICDPW contains 183 benchmarks for HGF, but some of them are without data, and some of those with data were without coordinates. We were able to approximately locate some benchmarks by comparing their positions on maps with their apparent locations on Google Earth displays. As a result, our current leveling data set for HGF consists of the annual surveys for 132 benchmarks, for the period 1994-2011. The reference point for these measurements is benchmark A-33.

Furthermore, we use modeled time series for 18 GPS stations (see Fig. 1) in the area, which were downloaded from the Scripps Orbit Permanent Array Center (SOPAC) website – http://sopac.ucsd.edu. Table 1 shows the three-component annual rates modeled for some of these stations. In this table *U* means up or down movements, with negative values indicating "down," or subsidence. *E* denotes the eastern horizontal component of deformation, with negative values indicating westward movements. *N* denotes the northern horizontal component, with negative values indicating southward movements. The table also shows offsets associated with the M7.2 event in April 2010 for all listed GPS stations, and with the M5.1 event in September 2005 at two GPS stations. The columns containing information for the *N*-component are grayed out, because these measurements are irrelevant to the SqueeSAR results. Only the *U*- and *E*-components are of significance to the SqueeSAR measurements. As a reminder, the GPS measurements are "absolute", whereas the SqueeSAR measurements are referenced to a point assumed to be motionless. GPS stations P503 on the Superstition Hills fault and DHLG near the San Andreas fault have been used as reference points.

Other data used for comparison are the relocated earthquake epicenters for the period January 1981 – June 2011 (Hauksson et al., 2012). We superimposed these on deformation maps from SSGF and looked at cross-sections in depth along profiles, either along or across linear features suggested by the earthquake epicenters (Eneva et al., 2012).

RESULTS

Most of the results are presented as deformation maps. The deformation rates in these maps are color-coded with "warm" colors (red and yellow) indicating negative movements and "cold" colors (blue) indicating positive movements. When LOS deformation is shown, this color coding indicates movements away from and toward the satellite, respectively. Since the look angle is steep, often LOS movements away from the satellite are indicative of subsidence, and toward the satellite – of uplift. The LOS movements are shown with numerous color-coded points, which are either PS (permanent scatterers) or DS (geometric centers of the distributed scatterers). These displays are produced with ArcGIS. In other cases, the movements are averaged over pixels of certain size. Here we use 200-m pixels. Such pixels can be used for presenting mean LOS movements (averaged from all individual PS and DS within the pixels), as well as decomposed vertical and east horizontal movements. The decomposed movements are always calculated from groups of ascending and descending LOS, and are thus assigned to the pixels containing these groups. It is not common to have individual points with both LOS measurements; due to the different viewing angles, the PS and DS from the two sets may be spatially close, but are not identical. Furthermore, we use simple linear interpolation through areas, for which there are no data, to obtain smoothed displays of LOS and decomposed movements. All plots showing mean and interpolated values are produced with Matlab codes, specifically developed for the analysis of the SquеSAR results. The color-coding is the same as for the individual LOS rates, although the maximum and minimum values may vary from plot to plot. Matlab codes are also used for extracting mean time series for polygons of interest, plots of annual rates along profiles, and depth cross-sections of earthquake hypocenters. Some examples follow.

Geothermal Fields

Salton Sea geothermal field – CalEnergy units

We have previously reported extensively on our findings in the Salton Sea geothermal field (SSGF) – area #1 in Fig. 2. Using two-year data from the Canadian satellite Radasat (Eneva et al., 2009; Eneva and Adams, 2010) and 8-year data from the European satellite Envisat (Eneva et al., 2012), two subsidence bowls were identified on the territory of the CalEnergy units of SSGF. Results were reported in reference to benchmark S-1246 (on Obsidian Butte), as it was used as a reference in the leveling surveys. This made it possible to make direct comparisons between the leveling data and the decomposed vertical movements from the satellite data. A very good agreement was noted both between the Radarsat and Envisat results, and the vertical deformation extracted from the satellite data and the leveling data provided by CalEnergy. In the larger subsidence bowl, the vertical movement was noted to be up to –30 mm/year. However, we established that the reference point, S-1246, subsides at about –20 mm/year, so the maximum absolute movement is even larger, up to –50 mm/year.

Eneva and Adams (2010) presented a discussion on the possible reasons for subsidence in the CalEnergy area of the SSGF. In summary, we estimated that at most 10% of the maximum deformation can be explained by the regional tectonics. CalEnergy indicates that only a small portion of the total geothermal resource has been exploited, and that minimal pressure changes and no fluid level changes have been detected in the wells. This leads to the suggestion that the reason for the observed surface deformation must be mostly local tectonics and not the geothermal operations.

Eneva et al. (2009, 2012) showed examples of deformation rates along profiles, in small areas including production and injection wells, as well as superimposed with seismicity. The reader is referred to those papers for details. Here Figure 3 illustrates the two subsidence bowls on both sides of the Brawley Seismic Zone (BSZ) and the superimposed earthquake epicenters. The reference point in this case is near GPS station DHLG to the north (see Fig. 1 for the location of DHLG).

Salton Sea geothermal field – Hudson Ranch - I development by Energy Source

Subsidence takes place beyond the limits of the CalEnergy units of the SSGF, where there has not been any production during the period of the satellite data (2003-2010). Figure 4 shows the non-interpolated LOS rates, which provide more detail than Fig. 3. Other than within the CalEnergy units

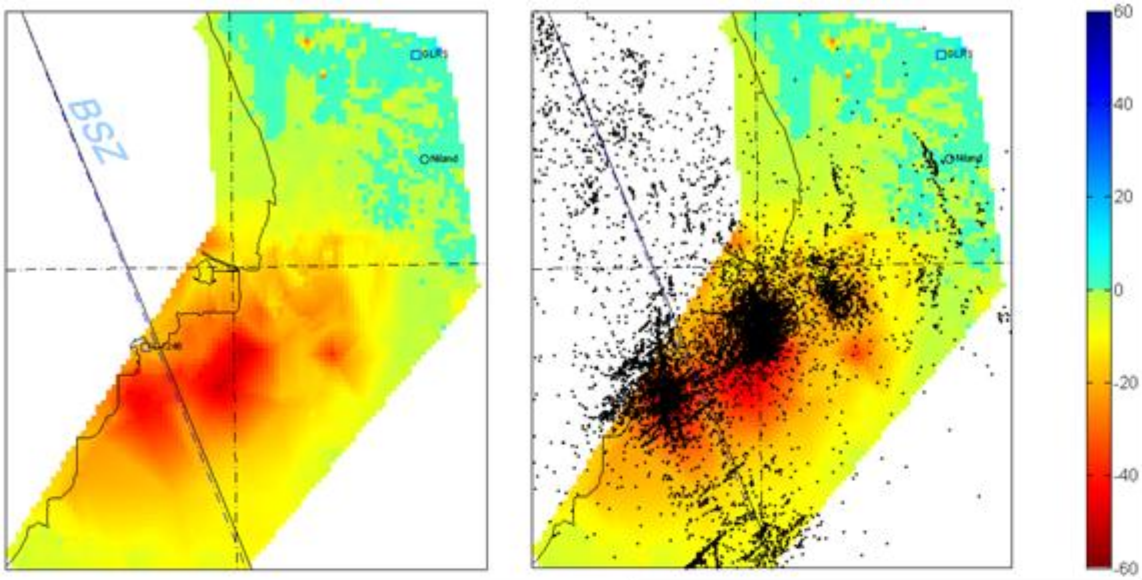

Figure 3. Interpolated ascending LOS rates using GPS station DHLG as a reference point. Straight line from NW to SE is the center of the Brawley Seismic Zone (BSZ). Rates are color-coded according to vertical bar, in mm/year. Two subsidence areas on both sides of the BSZ line are indicated with red color. Plot on the right shows superimposed relocated epicenters of M≥0.0 earthquakes for the period January 1981 – June 2011.

of the field, subsidence is also seen in the vicinity of the new power plant, Hudson Ranch - I (HR - I), although at a smaller rate. Fig. 4 also shows an injection well, three production wells, and the area, within which Energy Source will have to monitor the surface deformation and report the observations to the Imperial County (this is an obligation of all companies operating geothermal plants in Imperial Valley). The caption to Fig. 4 lists the maximum LOS rates at five individual areas, two of which are near HR - I. The subsidence decreases from the new development toward the northeast. Our SqueeSAR observations demonstrate the value of providing pre-production deformation baselines, which do not exist for the already operating plants at SSGF, HGF and EMGF. It is reasonable to assume that if significant changes to the baseline pattern of deformation occurs in the future, it might be caused by the operation of the HR - I development, and other plants to follow. If this is the case, such information could be used by Energy Source as a valuable feedback in its injection and production planning.

Heber geothermal field

The Heber geothermal field (HGF), operated by Ormat, is located close to the U.S. - Mexico border – area #3 in Fig. 2. To the best of our knowledge, the SqueeSAR results we presented earlier (Eneva et al., 2012) were the first of this kind for this field. In that case we showed two maps with color-coded ascending and descending LOS rates, indicating uplift in the northwestern part of the field and subsidence to the southeast, as well as examples of time series at individual PS points. The uplift-subsidence pattern was already known from the annual leveling surveys conducted by Ormat. However, the number of PS and DS points, at which we have obtained deformation time series, and hence estimates of annual rates, is much larger than the number of benchmarks used in the leveling surveys.

Figure 5 shows a map of interpolated LOS rates clearly indicating the pattern of uplift and subsidence mentioned above. The locations of the leveling benchmarks are also shown. The other plots in this figure show the annual rates along a profile transecting the uplift and subsidence areas, as well as mean deformation time series from those areas. The reference point is in the vicinity of GPS station P503 on the Superstition Hills fault (see Fig. 1 for its location). The following rates (mm/year) are calculated as the slopes of the time series shown in Fig. 5c-d. Uplift area: leveling = +12.2±1.7; ascending = +21.4±0.3; descending = +10.6±0.1; vertical = +16.0 ±0.2; east = –17.0±0.7. Subsidence area: leveling = –32.4±3.5; ascending = –38.7±0.2; descending = –18.9±0.3; vertical = –25.7±0.2; east = +11.8±0.8. The leveling rates are calculated for the period 2003-2010, for direct comparison with the SqueeSAR results, even though the plots show earlier leveling measurements as well. Of these rates, only the leveling and the vertical rates can be compared directly. They appear within 4 and 6 mm/year, respectively, but should be still considered close enough, as the SqueeSAR results are averaged over the polygons shown in Fig. 5a, while the leveling measurements are from benchmarks at specific points within these polygons. Also notable are the decomposed horizontal movements, westward in the uplift area and eastward in the subsidence area.

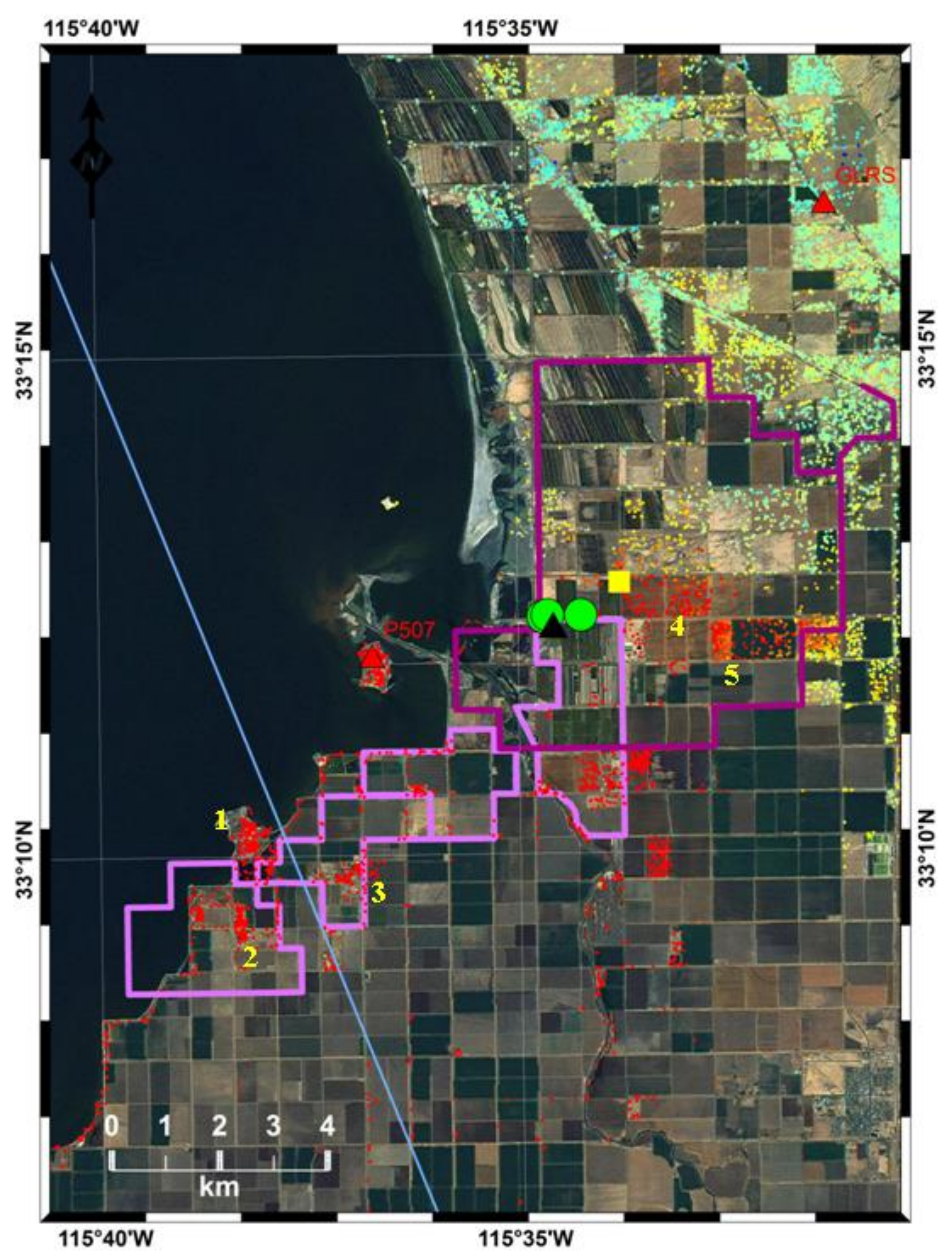

Figure 4. Salton Sea geothermal field area. Pink polygons show CalEnergy units. The new Hudson Ranch – I development operated by Energy Source is shown with its power plant (black triangle), production wells (green circles), and an injection well (yellow square). Dark red outline shows the area, which Energy Source will have to monitor for subsidence. Colored points are PS and DS, with red and yellow colors indicating ascending LOS movements away from the satellite and blue colors showing movements toward the satellite. The reference point is near GPS station DHLG (to the northwest, outside of this map). Maximum LOS rates at some areas are: 1 – up to –50 mm/yr; 2 – up to –22 mm/yr; 3 – up to –40 mm/yr; 4 – up to –16 mm/yr; 5 – up to –13 mm/yr (all away from satellite indicative of subsidence).

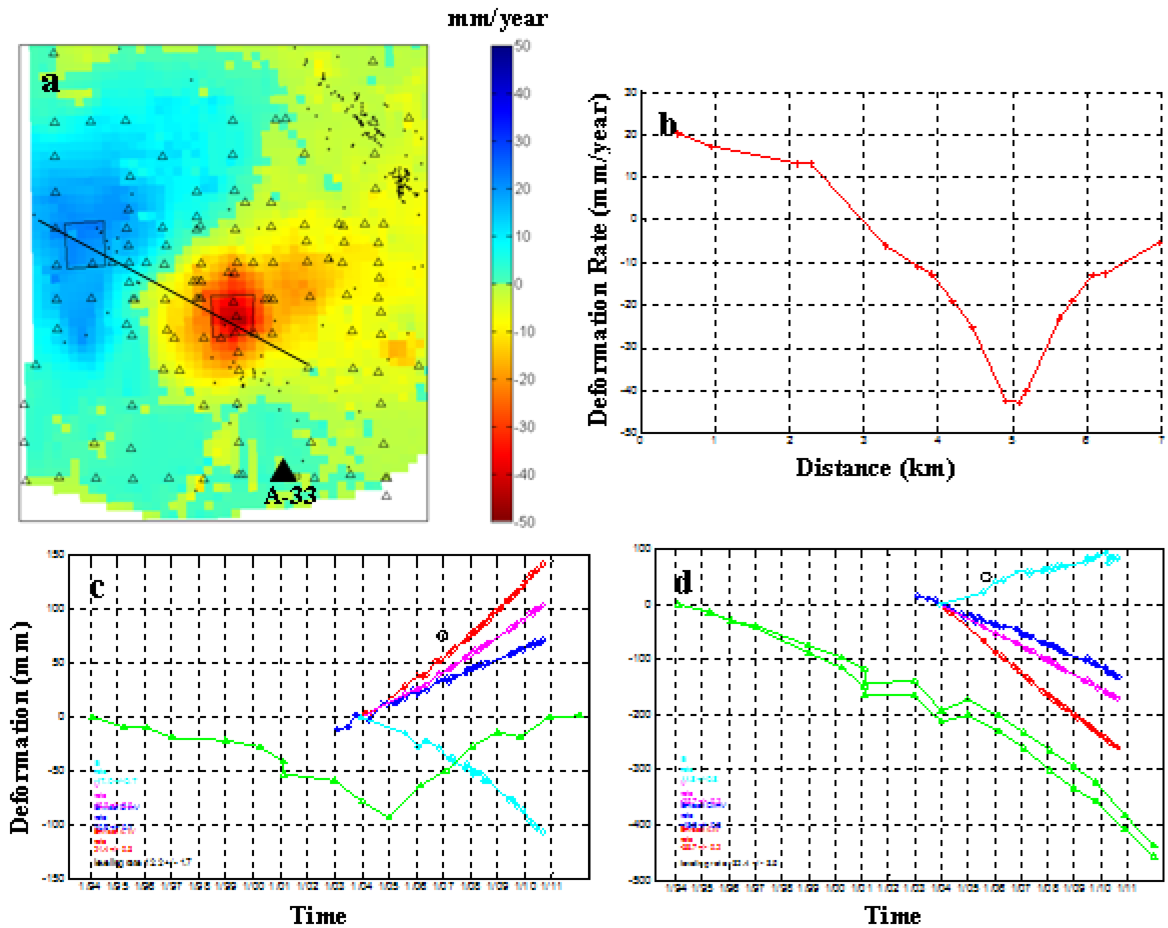

Figure 5. Example of deformation along a profile and mean deformation rates within polygons from Heber. (a) Map of interpolated LOS ascending deformation rates (in mm/year) referenced to leveling benchmark A-33 (solid black triangle). Locations of other leveling benchmarks are shown with smaller empty triangles. Rates are color coded as shown by vertical bar to the right of the map. Small crosses show M≥0 earthquake epicenters for the period January 1981-June 2011. Straight black line in the NW-SE direction shows a profile, along which LOS ascending deformation rates are illustrated in (b). Mean deformation time series (in mm) for the area outlined with black polygon in the uplift area (western part of map) are shown in (c), and for the polygon in the subsidence area (central part of map) in (d). Green lines and symbols show time series at leveling benchmarks within the polygons. Red and dark blue lines and symbols show mean LOS deformation series from the ascending and descending data, respectively. Pink and light blue symbols and lines show decomposed time series indicating mean vertical and east horizontal movements, respectively. Circles in (c) and (d) show times of earthquakes in the respective polygons.

East Mesa geothermal field

We reported on the EMGF earlier (Eneva et al., 2012). This field (#4 in Fig. 2) is outside the agricultural part of the study region, so the conventional DInSAR approach works very well and results have been reported earlier by Massonnet et al. (1997). These authors used four pairs of descending scenes from the ERS-1 satellite (a predecessor of Envisat), in the period 1992-1994. A maximum subsidence rate of –35 mm/year was estimated at that time.

Because the area occupied by the EMGF is arid, the density of PS and DS points in our SqueeSAR application is very high. Most of the area is subjected to subsidence, with a maximum LOS ascending rate of –29 mm/year (using P503 as a reference point, the same as for HGF). The EMGF is clearly outlined in one of the subsequent figures, Figure 9 (in the next section discussing the effect of faults).

North Brawley geothermal field

This field (#2 in Fig. 2) started operation at the

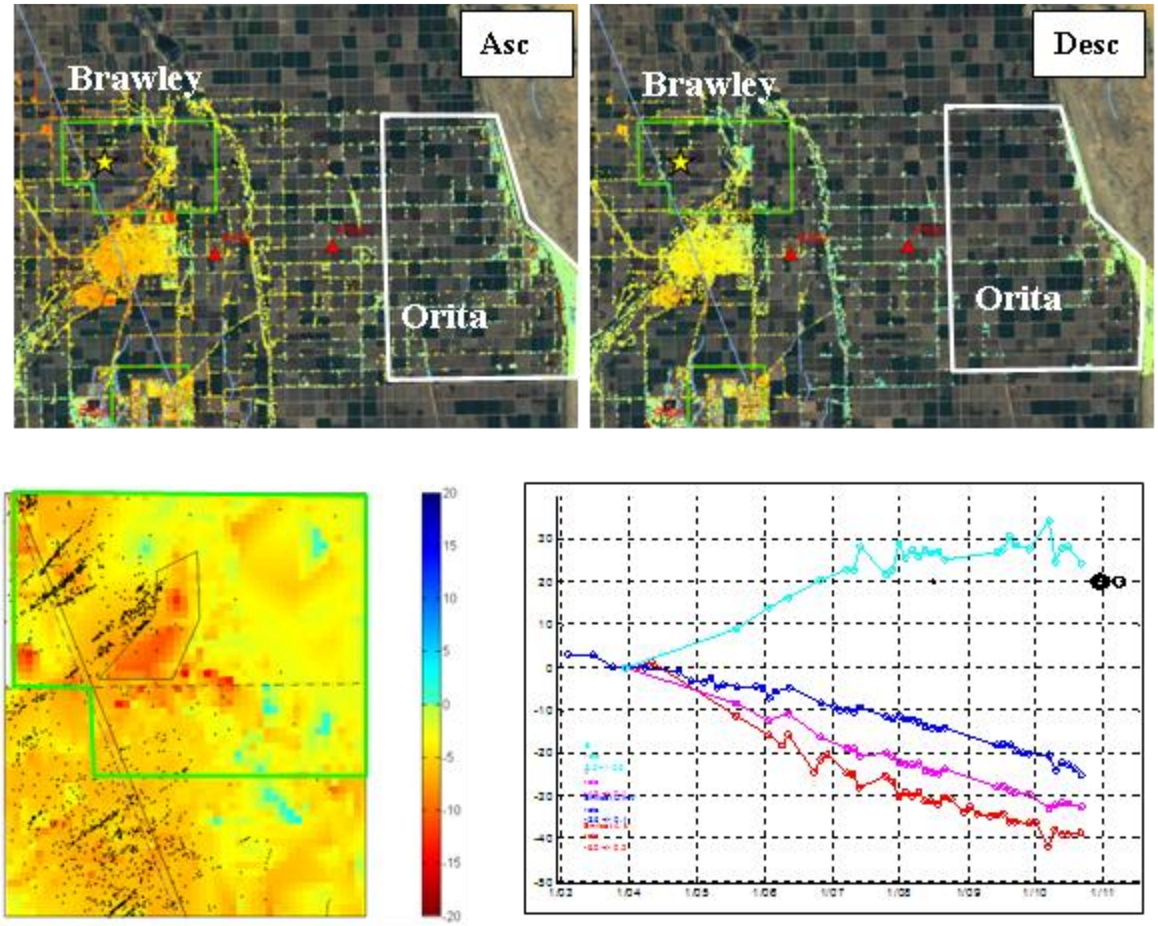

Figure 6. Example from the North Brawley geothermal field and the prospective area of Orita. Top – the North Brawley and Orita areas are marked with green and white polygons, respectively. The ascending (left) and descending (right) LOS rates are color-coded . Yellow star in the Brawley area marks the location of the M5.4 earthquake swarm that occurred in August 2012. Bottom left – zoom in the North Brawley area, showing interpolated LOS ascending rates, color-coded as shown by vertical bar, in mm/year. Black dots mark earthquake epicenters for the period January 1981 – June 2011. Black polygon outlines area of apparent largest movements away from the satellite in this area, for which mean time series are shown to the right. Bottom right – mean deformation time series for: descending LOS (dark blue); ascending LOS (red); and decomposed vertical (pink) and east horizontal (light blue) movements. Black circles show times of earthquakes.

end of the study period (2003-2010), so along with Hudson Ranch – I, it is another example where collection of pre-operational baseline deformation is possible. Figure 6 shows maps of the ascending and descending LOS movements, with more information about one particular polygon outlining an area of enhanced LOS movements away from the satellite. The annual rates evaluated from the mean time series, shown in Fig. 6, are: descending = -3.6 ± 0.1, ascending = -6.0 ± 0.2, vertical = -4.8 ± 0.1, and east = $+3.5 \pm 0.5$ mm/year, respectively.

Other areas with geothermal potential

Other areas of geothermal potential include those of interest to the U.S. Navy Geothermal Program Office (GPO). These are the areas near Superstition Hills and Superstition Mountain faults to the west (#5 in Fig. 2) and the Hot Springs fault near Chocolate Mountains to the northeast (#6 in Fig. 2). The former will be discussed in more detail in the next section describing the effects of faults on the deformation field. In addition, the area of Orita (East Brawley) has been also of geothermal interest (#7 in Fig. 2). LOS ascending and descending results for it can be seen in Fig. 6, east of the NBGF.

Faults

The surface deformation measurements from SqueeSAR show clear differential displacements on both sides of some faults. Figure 7 shows the area of the Superstition Hills fault. It is clearly identified based on systematic differences in deformation on both sides. These differences are of only a few mm/year, but are sufficient to show a clear contrast.

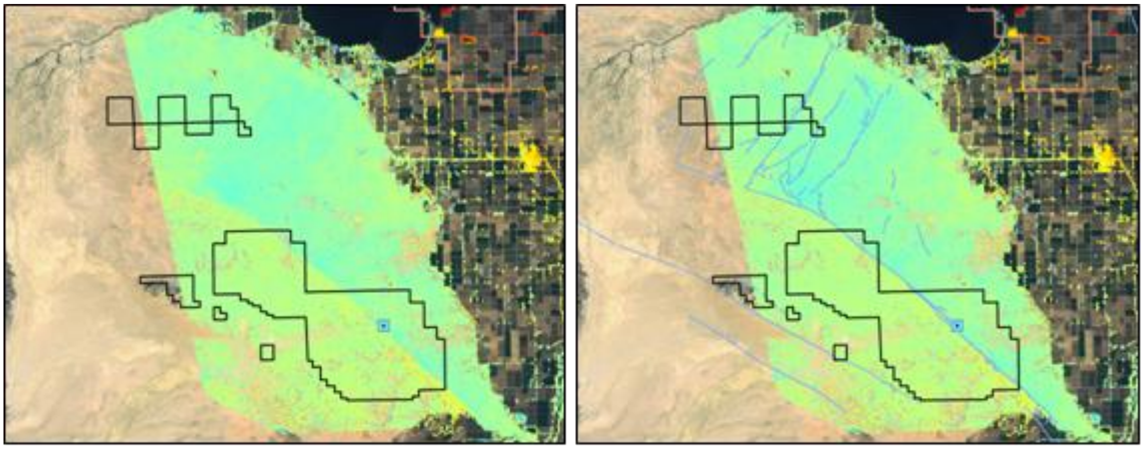

Figure 7. Descending LOS deformation rates in the area of Superstition Hills fault. Plot on the right shows with blue lines superimposed fault traces. Black polygons show areas of geothermal interest to the U.S. Navy GPO. Blue square marks reference point near GPS station P503.

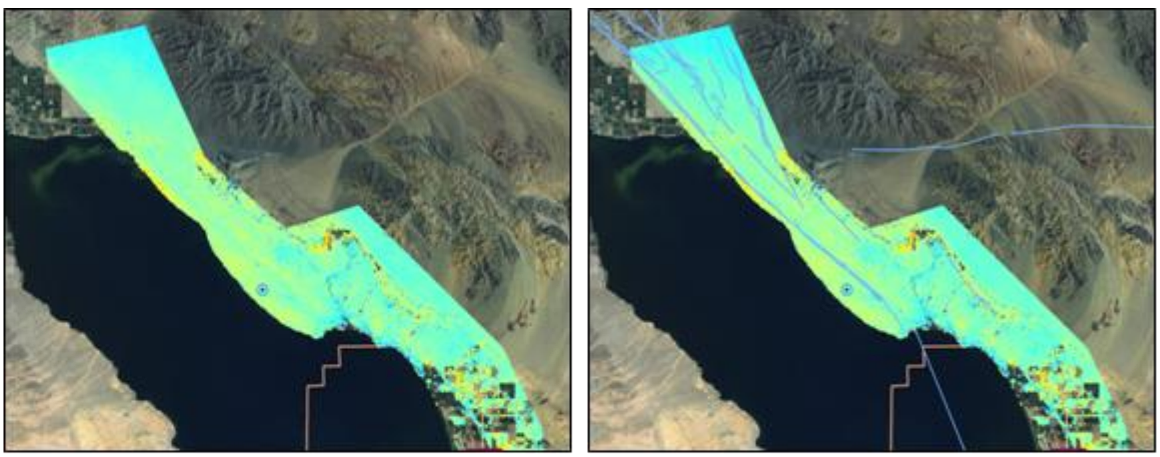

Figure 8. Descending LOS deformation rates in the area of San Andreas fault. Plot on the right shows with blue lines superimposed fault traces. Blue circle marks reference point near GPS station DHLG. Pale pink outline marks part of the Salton Sea KGRA

.

Decomposition into the vertical and the east horizontal components makes the difference even clearer, as demonstrated in the next section, discussing the effects of an earthquake and aseismic event on this fault. The reference point in this case is near GPS station P503. Similar differentiation is seen for some portions of the San Andreas fault (Figure 8), with a reference point near GPS station DHLG. Although significant, these results are not particularly unique, because these faults traverse relatively dry areas, and the traditional DInSAR technique can be also used to outline them, as demonstrated by Wei et al., 2009, 2011).

However, our results showing the delineation of the Imperial fault (Figure 9) are unique, because DInSAR does not work in this agricultural area, and only the SqueeSAR technique is capable of extracting this type of information. In this case the distribution of PS points is not as dense, as those along the Superstition Hills and the San Andreas faults, and is confined mostly to streets and canals. Nonetheless, the contrast is obvious.

Effect of Earthquakes and Aseismic Events

Wei et al. (2009) describe the effect on the Superstition Hills fault of an October 2006 aseismic event of equivalent moment magnitude Mw~4.7, which was recorded by a creep meter. Furthermore, they report effects of a more distant M7.2 earthquake in April 2010 on several faults in the area (Wei et al., 2011). In both cases DInSAR was used to detect these effects. GPS stations have also recorded fault offsets associated with the M7.2 event (see Table 1). However, GPS station P503 on the Superstition Hills fault, not far from the creep meter recording the

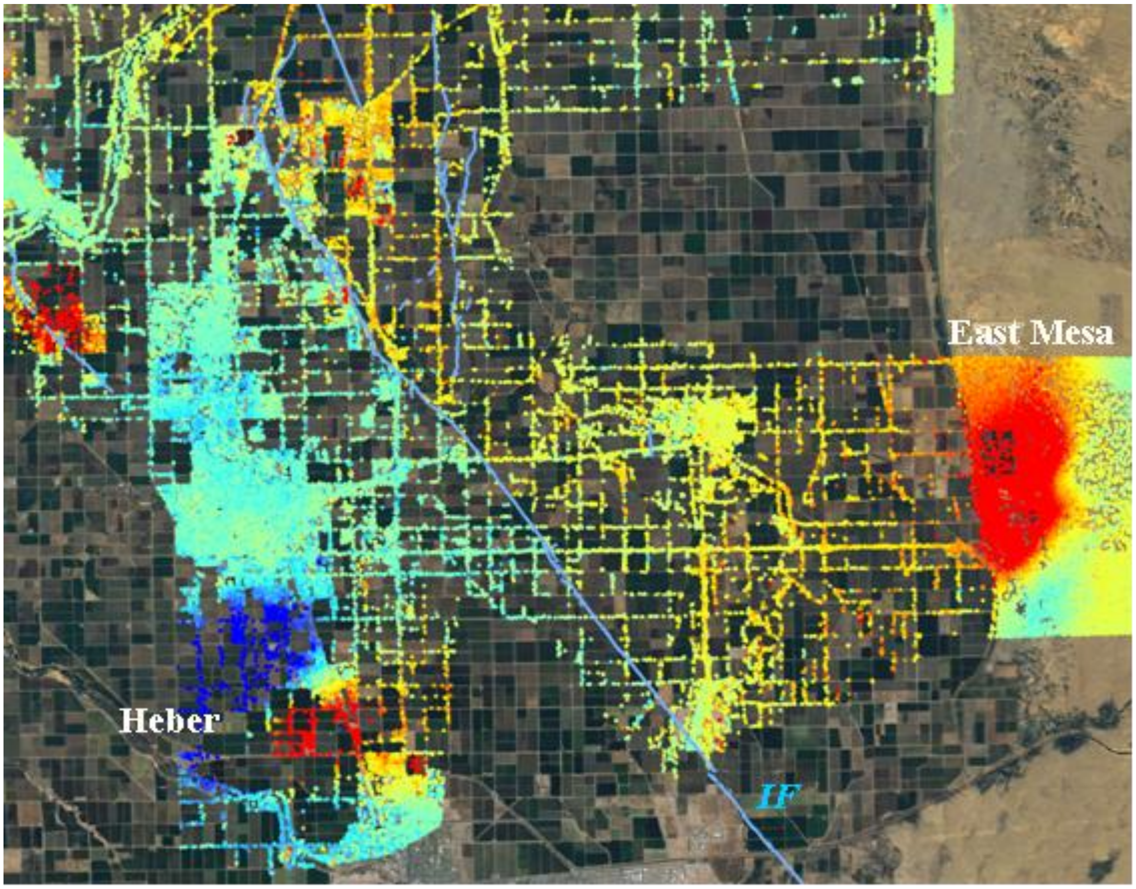

Figure 9. Ascending LOS deformation rates in the southern part of the study region, referenced to GPS station P503 (northwest from the mapped area). Fault traces are marked with blue lines. The highest rates are seen in the Heber and East Mesa geothermal field, but the Imperial fault (IF) also marks a contrast in the surface deformation field

.

October 2006 aseismic event, was not operating yet at that tome, so this event was not recorded by any GPS stations.

Figure 10 shows the mean vertical and horizontal movements as derived from the SqueeSAR measurements in two pairs of polygons on both sides of the Superstition Hills fault, with a reference point to the northeast of the fault. While not much movement is detected in the polygons on that same side of the fault (A and B in Fig. 10), significant westward component is seen in the two polygons on the other side of the fault (C and D). Also, two steps are seen in the mean time series indicating westward movement, at the times of the aseismic event and the M7.2 earthquake. The "jumps" associated with the aseismic event are measured at 10 and 7 mm westward in polygons C and D, respectively. The effect of the M7.2 earthquake is measured at 12 and 10 mm offsets westward in those same polygons. It is to be noted that such effects are difficult to detect in time series for individual PS points, because they are rather noisy, and this is the reason to look at mean time series within large enough areas to have a good representation from a number of individual time series, but small enough for the time series to represent similar amounts of changes in surface deformation. This consideration is particularly valid for decomposed time series (vertical and horizontal), as they are averaged by default within pixels of some size.

Figure 11 shows another representation of the effect of these events. It shows the surface deformation as it progresses in time along a profile transecting the Superstition Hills fault southwest of the creep meter. The two events are detectable in this rendition of the SqueeSAR results as well. The effect is particularly clear if shown as animation. Further northwest along this fault, the effect of the M7.2 event is still detectable, but the effect of the aseismic event disappears (not shown in Fig. 11).

Results in other parts of the study region are more ambiguous. For the area around Imperial fault, we look at the offsets measured at some GPS stations at the time of the M7.2 event. We calculate these in reference to P503, as it is the reference point for the

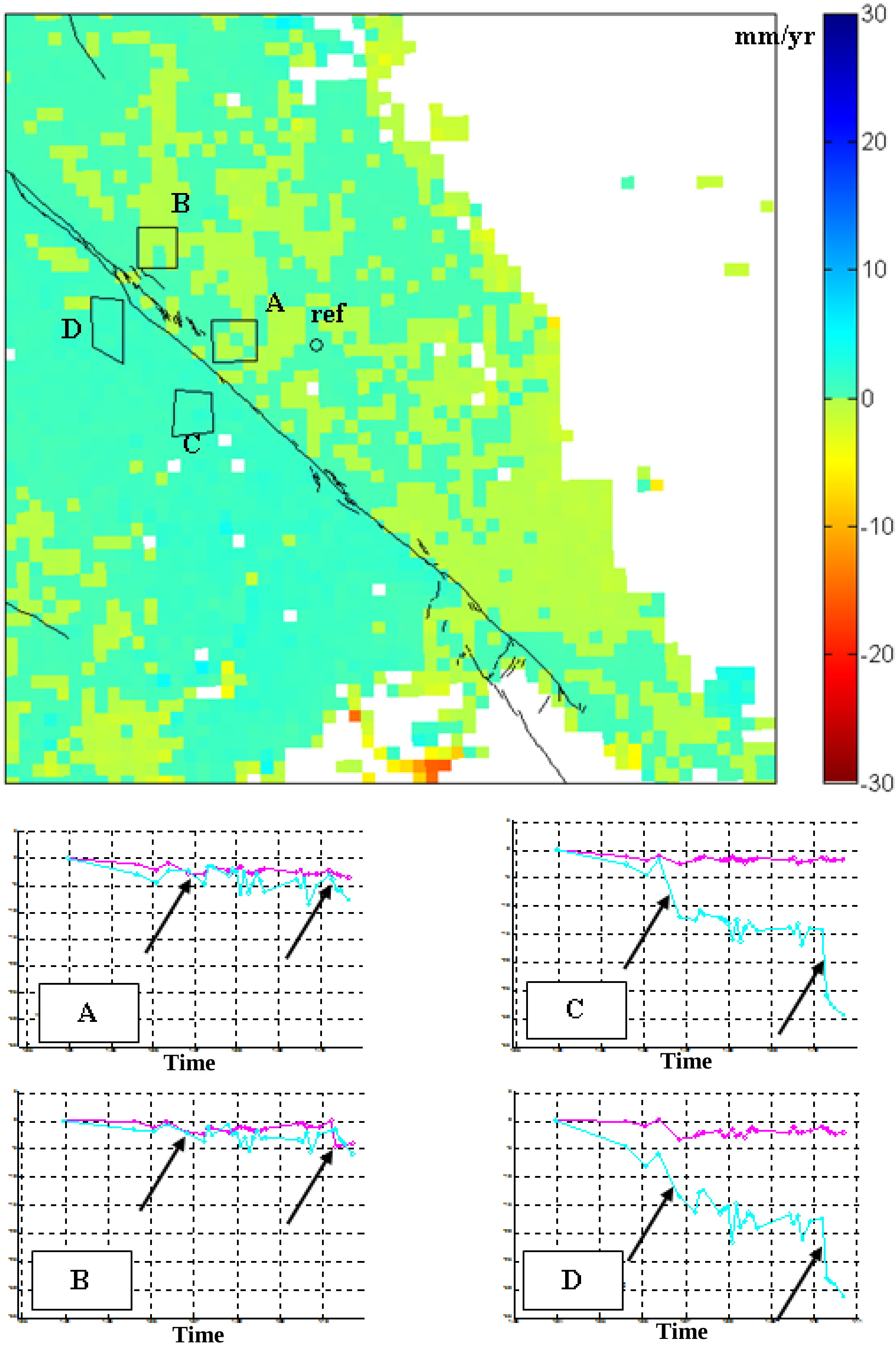

Figure 10. Color-coded mean LOS ascending rates from four polygons around the Superstition Hills fault. Red and yellow colors indicate movements away from the satellite and blue colors – toward the satellite, in mm/year. Circle (ref) marks reference point. Polygons are chosen on both sides of the fault and are marked with A, B, C, and D. These same letters mark the corresponding plots showing mean time series of the decomposed vertical (pink) and east (light blue) horizontal movements, in mm, derived from individual LOS time series within the polygons. Arrows show the times of the October 2006 aseismic event and the April 2010 M7.2 earthquake.

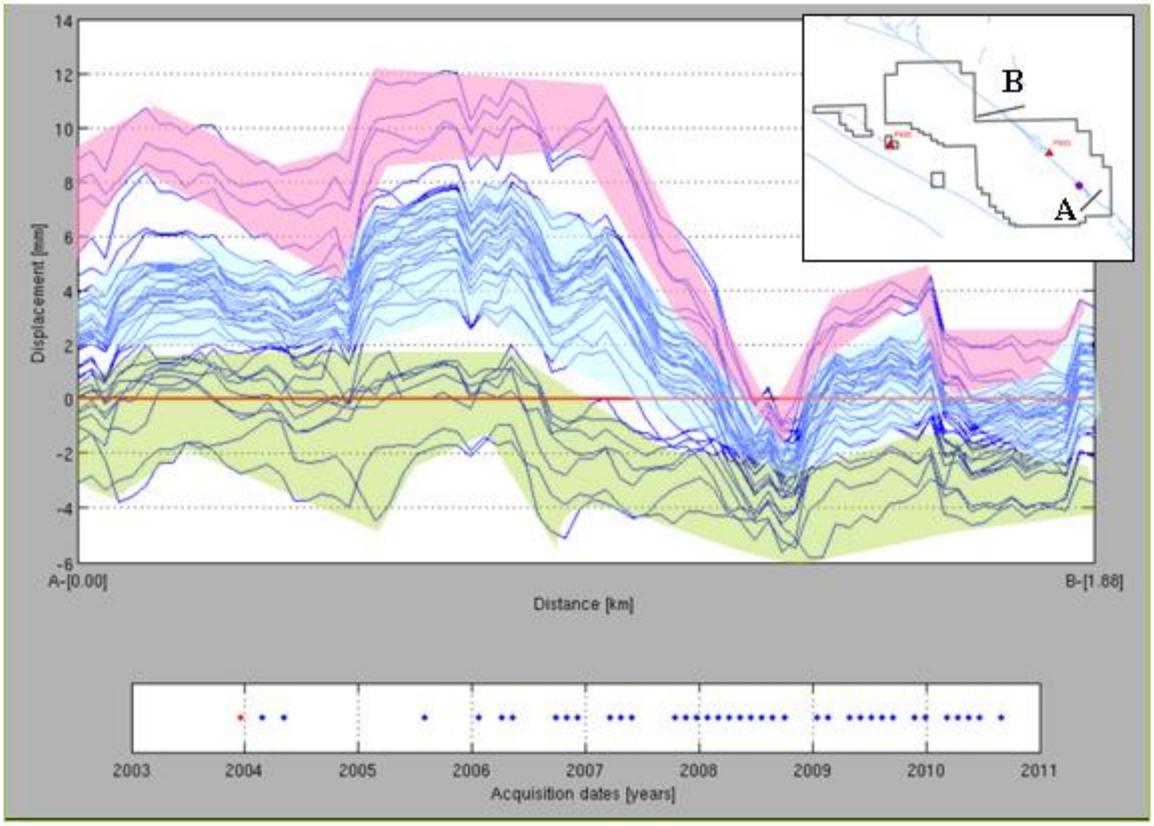

Figure 11. Cumulative LOS ascending deformation along a ~2 km profile (A) intersecting the Superstition Hills fault to the southeast of the creep meter detecting the aseismic Mw4.7 event in October 2006 (see inset in upper right corner for location of profile A). The times of the individual scenes are marked in the bar under the plot. Deformation curves progress in time from the bottom up, with each deformation curve corresponding to a time marked with a dot in the time bar. For example, the first curve on the bottom marks deformation in the second scene (02/24/2004) compared with the first one (12/16/2003 – red dot in time bar), and the top curve shows the deformation reflected in the last scene (8/31/2010) compared to the last-but-one scene (6/22/2010). Three clusters of deformation curves are seen in time. The initial cluster (green), reflecting the natural spatial heterogeneity along the profile, "jumps" to a second cluster (blue) after the October 2006 aseismic event, which in turn shifts to a third cluster (pink) after the M7.2 event in April 2010. A deformation progression along profile B to the north also indicates a change after the 2010 M7.2 event, but the 2006 aseismic event does not have a detectable effect anymore (not shown).

SqueeSAR results in this area. These differences show what changes might be expected, as seen in Table 2. The table shows vertical changes up to 8 mm

Table 2. Differences from P503

GPS Stat	Diff N	Diff E	Diff U
P498	7.1	5.8	-6.8
P497	36.2	0.8	-8.0
P496	119.4	-14.2	1.6
P500	-5.6	-52.3	2.8
P493	-26.2	11.2	3.2

and westward changes of up to 14 mm (P500 shows a larger horizontal difference, but it is not in the area covered by SqueeSAR). See Fig. 1 for the locations of the GPS stations. We will continue looking at details of the SqueeSAR measurements, but so far have no convincing indication that the effect of the M7.2 earthquake can be easily discerned in our results for this area.

Another earthquake that might be expected to have had some local effect on surface deformation is the M5.1 event in September 2005 on the territory of the Salton Sea geothermal field. Lohman amd McGuire (2007) have observed a 14-cm peak-to-peak LOS change associated with it, using conventional DInSAR technique. Although it cannot work in agricultural areas to detect ongoing smaller deformation, in that particular case the authors used a pair of consecutive scenes from track 84 (different from our data), which were only 35 days apart. Decorrelation had not occurred in the epicentral area for such a short period of time, and the large signal from the earthquake was readily detected. However, in our case, scenes spanning the time of this event cover longer periods (70 days for the descending and 175 days for the ascending), and because of decorrelation and lack of PS points in the exact area of the epicenter, our time series do not detect the M5.1 event.

CONCLUSIONS

The InSAR technique used here, SqueeSAR™, has provided unprecedented information on surface deformation in Imperial Valley. Except for the area of the East Mesa geothermal field, no other InSAR techniques could work in most of the geothermal fields of this region, because of extensive agriculture. The spatial details revealed cannot be achieved by any ground-based means, such as GPS and leveling. This type of results is invaluable with its capability to provide deformation baselines for future geothermal fields in the area. In addition, such results are very informative for the improved understanding of surface deformation in current fields. Furthermore, they can be used to outline faults and to detect effects of aseismic and seismic events. Thus radar interferometry can find applications in pre-production reservoir assessment, ongoing exploration to determine drilling targets, mitigation of any environmental impact that may occur from geothermal operation, and detection of ongoing and abrupt fault movements.

ACKNOWLEDGEMENTS

Support from the Geothermal Grants and Loans Program of the California Energy Commission (CEC), Grant GEO-10-001, is gratefully acknowledged. Many thanks to Alex Schriener and Jon Trujillo from CalEnergy for assuring match share to the CEC grant in the form of digital data from the annual leveling surveys at the Salton Sea geothermal field, and helping with the interpretation of the InSAR results. The Imperial County Department of Public Works (ICDPW) is thanked for providing digital data for the leveling surveys at the Heber geothermal field. Danny Sims and Jim Turner from Energy Source are thanked for providing insight and information on the new development at the Salton Sea geothermal field, Hudson Ranch - I. We thank Fabrizio Novali and Jacopo Allievi from TRE Italy for extensive discussions about the application of the SqueeSAR technique and for providing Fig. 11. The Envisat satellite data were obtained from the European Space Agency (ESA) as part of an approved Category-1 research data proposal. GPS data are from the Scripps Orbit Permanent Array Center (SOPAC) website – http://sopac.ucsd.edu.

REFERENCES

Ben-Zion, Y. and Lyakhovsky, V. (2006), “Analysis of Aftershocks in a Lithospheric Model with Seismogenic Zone Governed by Damage Rheology,” *Geophysical Journal International*, **165**, 197– 210.

Brothers, D. S., Driscoll, N. W., Kent, G. M., Harding, A. J., Babcock, J. M. and Baskin, R. L. (2009), “Tectonic Evolution of the Salton Sea Inferred From Seismic Reflection Data,” *Nature Geoscience*, **2**, 581-584, doi: 10.1038/ NGEO590.

Carnec, C. and Fabriol, H. (1999), “Monitoring and Modeling Land Subsidence at the Cerro Prieto Geothermal Field, Baja California, Mexico, Using SAR Interferometry,” *Geophysical Research Letters*, **26**, 1211-1214.

Eneva, M., Falorni, G., Teplow, W., Morgan, J., Rhodes, G. and Adams, D. (2011), “Surface Deformation at the San Emidio Geothermal Field, Nevada, from Satellite Radar Interferometry,” *Geothermal Resources Council Transactions*, **35**, 1647-1653.

Eneva, M. (2010), “Detection of Surface Deformation at Mining and Geothermal Sites Using Satellite Radar Interferometry (InSAR),” in *Proceedings of the 44th U.S. Rock Mechanics Symposium and 5th U.S.-Canada Rock Mechanics Symposium, Salt Lake City, June 27-30, 2010*.

Eneva, M. and Adams, D. (2010), “Modeling of Surface Deformation from Satellite Radar Interferometry in the Salton Sea Geothermal Field, California,” *Geothermal Resources Council Transactions*, **34**, 527-534.

Eneva, M., Falorni, G., Adams, D., Allievi, J. and Novali, F. (2009), “Application of Satellite Interferometry to the Detection of Surface Deformation in the Salton Sea Geothermal Field, California,” *Geothermal Resources Council Transactions*, **33**, 315-319.

Falorni, G., Morgan, J. and Eneva, M. (2011), “Advanced InSAR Techniques for Geothermal Exploration and Production,” *Geothermal Resources Council Transactions*, **35**, 1661-1666.

Ferretti, A., Prati, C. and Rocca, F. (2000), “Nonlinear Subsidence Rate Estimation Using Permanent Scatterers in Differential SAR Interferometry,” *IEEE Tranctions on Geoscience and Remote Sensing*, **38**, 2202-2212.

Ferretti, A., Savio, G., Barzaghi, R., Borghi, A., Musazzi, S., Novali, F., Prati, C. and Rocca, F. (2007), “Submillimeter Accuracy of InSAR

Time Series: Experimental Validation," *IEEE Transactions on Geoscience and Remote Sensing*, **45**, 1142-1153.

Ferretti, A., Fumagalli, A., Novali, F., Prati, C., Rocca, F. and Rucci, A. (2011), "A New Algorithm for Processing Interferometric Data-Stacks: SqueeSAR," *IEEE Transactions on Geoscience and Remote Sensing*, **49** (9), 3460-3470.

Fialko, Y. and Simmons, M. (2000), "Deformation and Seismicity in the Coso Geothermal Area, Inyo County, California: Observations and Modeling Using Satellite Radar Interferometry," *Journal of Geophysical Research*, **105**, 21,781-21,793.

Hauksson, E., Yang, W. and Shearer, P. M. (2012), "Waveform Relocated Earthquake Catalog for Southern California (1981 to 2011)," *Bulletin of Seismological Society of America*, **102** (5), 2239-2244, doi: 10.1785/0120120010.

Lohman, R. B. and McGuire, J. J. (2007), "Earthquake Swarms Driven by Aseismic Creep in the Salton Trough, California, "*Journal of Geophysical Research.*, **112**, B04405, doi:10. 1029/2006JB 004596.

Massonnet, D., Holzer, T. and Vadon, H. (1997), "Land Subsidence Caused by the East Mesa Geothermal Field, California, Observed Using SAR Interferometry," *Geophysical Research Letters*, **24** (8), 901–904, doi:10.1029/ 97GL00817.

Oppliger, G., Shevenell, L. and Coolbaugh, M. (2008), "Preliminary Site Assessment of the Redfield Campus, Reno, NV, USA." *Geothermal Research Council Transactions*, **32**, 163-168.

Rymer, M. J., Boatwright, J., Seekins, L. C., Yule, J. D. and Liu, J. (2002), Triggered Surface Slips in the Salton Trough Associated with the 1999 Hector Mine, California, Earthquake, *Bulletin of the Seismological Society of America*, **92**, 13001317, doi:10.1785/0120000935.

U.S. Geological Survey (California Geological Survey), (2006), "Quaternary Fault and Fold Database for the United States," accessed October 2011, from USGS web site: http//earthquakes.usgs.gov/regional/qfaults.

Wei, M., Sandwell, D. and Fialko, Y. (2009), "A Silent Mw 4.7 Slip Event of October 2006 on the Superstition Hills Fault, Southern California," *Journal of Geophysical Research*, **114**, B07402, doi:10.1029/2008JB006135.

Wei, M., Sandwell, D., Fialko, Y. and Bilham, R. (2011), Slip on Faults in the Imperial Valley Triggered by the 4 April 2010 Mw 7.2 El Mayor-Cucapah Earthquake Revealed by InSAR, *Geophysical Research Letters*, **38**, L01308, doi:10.1029/2010GL045235.

Wicks, C., Tatcher, W., Monastero, F. and Hasting, M. (2001), "Steady-State Deformation of the Coso Range, East-Central California, Inferred from Satellite Radar Interferometry, *Journal of Geophysical Research*, **106**, 13,769-13,780.